

Explainable Convolutional Neural Networks for Retinal Fundus Classification and Cutting-Edge Segmentation Models for Retinal Blood Vessels from Fundus Images

Fatema Tuj Johora Faria^{1*}, Mukaffi Bin Moin¹, Pronay Debnath¹,
Asif Iftekher Fahim¹, Faisal Muhammad Shah¹

¹*Department of Computer Science and Engineering, Ahsanullah
University of Science and Technology, Dhaka, Bangladesh.

*Corresponding author(s). E-mail(s): fatema.faria142@gmail.com;
Contributing authors: mukaffi28@gmail.com;
pronaydebnath99@gmail.com; fahimthescientist@gmail.com;
faisal.cse@aust.edu;

Abstract

Our research focuses on the critical field of early diagnosis of disease by examining retinal blood vessels in fundus images. While automatic segmentation of retinal blood vessels holds promise for early detection, accurate analysis remains challenging due to the limitations of existing methods, which often lack discrimination power and are susceptible to influences from pathological regions. Our research in fundus image analysis advances deep learning-based classification using eight pre-trained CNN models. To enhance interpretability, we utilize Explainable AI techniques such as Grad-CAM, Grad-CAM++, Score-CAM, Faster Score-CAM, and Layer CAM. These techniques illuminate the decision-making processes of the models, fostering transparency and trust in their predictions. Expanding our exploration, we investigate ten models, including TransUNet with ResNet backbones, Attention U-Net with DenseNet and ResNet backbones, and SwinUNET. Incorporating diverse architectures such as ResNet50V2, ResNet101V2, ResNet152V2, and DenseNet121 among others, this comprehensive study deepens our insights into attention mechanisms for enhanced fundus image analysis. Among the evaluated models for fundus image classification, ResNet101 emerged with the highest accuracy, achieving an impressive 94.17%. On the other end

of the spectrum, EfficientNetB0 exhibited the lowest accuracy among the models, achieving a score of 88.33%. Furthermore, in the domain of fundus image segmentation, Swin-UNET demonstrated a Mean Pixel Accuracy of 86.19%, showcasing its effectiveness in accurately delineating regions of interest within fundus images. Conversely, Attention U-Net with DenseNet201 backbone exhibited the lowest Mean Pixel Accuracy among the evaluated models, achieving a score of 75.87%. The presented findings contribute valuable insights to the performance and interpretability of deep learning models in fundus image analysis, offering advancements in medical image understanding and diagnosis.

Keywords: Fundus Images; Medical Imaging; Class Activation Map; Explainability; Retinal Image Segmentation; Convolutional Neural Network; Semantic Segmentation; Deep Learning

1 Introduction

The retina, choroid, photoreceptor cells, blood vessels, and optic nerve are all located in the fundus, which is the posterior region of the eye. An essential tool in the toolbox of ophthalmologists and other medical professionals is retinal fundus imaging, which makes it easier to identify and track vision-threatening eye disorders throughout time. This advanced method is essential for the diagnosis and treatment of conditions including diabetic retinopathy, glaucoma, and age-related macular degeneration (AMD) [1] [2] [3]. The chronic and degenerative eye illness known as AMD affects the macula, which is essential for clear vision. AMD, a common condition in the elderly, is characterized by abnormal blood vessel formation in wet AMD and drusen deposition in dry AMD. It is now the primary cause of vision loss. Known as the “silent thief of sight,” glaucoma is characterized by elevated intraocular pressure that can take many different forms. To avoid damage to the optic nerve, early diagnosis is crucial. Diabetes-related retinopathy (DR) is a condition that damages the retinal blood vessels. It increases the chance of blindness and visual impairment, hence early treatment is essential [4] [5].

Diagnosing diabetic retinopathy, glaucoma, and AMD involves an integrated approach that includes clinical evaluations and sophisticated imaging. Fundus photography provides highly precise images of the retina, while optical coherence tomography (OCT) offers cross-sectional views that facilitate the identification of macular abnormalities. Measurements of intraocular pressure, eye tests, and OCT assess structural changes in glaucoma [6]. The diagnosis of diabetic retinopathy includes retinal vascular abnormalities being highlighted by fluorescein angiography, fundus photography, and OCT for macular examination. Automated grading systems facilitate efficient screening, emphasizing the importance of regular eye examinations for early detection and timely intervention.

The diagnosis and continuous monitoring of common eye illnesses are revolutionized by the quick advances in artificial intelligence (AI)-based image identification and grading [7] [8]. Given that eye issues frequently do not show any symptoms at first, it is critical to step up efforts to semi-automate mass screening programs in order to identify diseases early and conduct routine monitoring. With quick treatments to avoid

visual damage or blindness, screening efficiency, efficacy, and financial viability will all be improved by this automation. AI integration has great potential to transform the manual categorization of retinal fundus images and bring about improved ophthalmology diagnostic capabilities [9]. In the realm of retinal vascular segmentation for medical imaging, the two predominant approaches, supervised and unsupervised methods, play a crucial role in automating the intricate task, substantially reducing time and effort compared to manual segmentation, particularly in addressing conditions like diabetic retinopathy, a leading cause of blindness [10] [11]. Despite significant progress enabled by modern imaging techniques, challenges persist in this domain, highlighting historical difficulties faced by ophthalmologists. Convolutional neural networks (CNNs) have emerged as a pivotal tool, although their operation as “black boxes” underscores the pressing need for understanding CNN layers. This understanding becomes especially relevant when integrating Explainable AI (XAI) strategies in the categorization of retinal fundus images, where transparency and interpretability are paramount. XAI, elucidating the decision-making processes of machine learning models, enhances the interpretability of CNN layers, contributing to the advancement of automated analysis techniques and, ultimately, improving medical diagnostics [12].

In recent years, substantial progress has been made in the domain of automatic retinal vessel segmentation and classification of fundus images, with notable contributions from several experts. Yeonwoo et al. [1] employed a CNN to effectively classify fundus image laterality, achieving an impressive 99% training accuracy across a substantial dataset of 25,911 images. By incorporating activation maps, particularly GradCAM, the study enhanced interpretability, aligning with clinicians’ attention. However, the research solely focused on GradCAM without delving into other advanced XAI techniques, leaving potential avenues for further investigation. Similarly, Yong et al. [9] utilized CNN models to predict age and sex accurately based on retinal characteristics, shedding light on the intricate relationship between retinal features and systemic conditions. While the study revealed lower R2 values in subgroups with health conditions, indicating varied features in aging and pathologic vascular changes, it also limited its exploration to GradCAM without considering other advanced XAI techniques. In the realm of ophthalmological diagnostics, Yuhang et al. [2] demonstrated the potential of deep learning with Inception V3 and ResNet-50 models in categorizing fundus images into crucial classes with remarkable accuracy. Despite their success, the absence of exploration into XAI techniques alongside model implementations underscored a missed opportunity to provide insights into the decision-making process, which could have bolstered transparency and trust in diagnostic outcomes. Advancing the field further, Chen et al. [13] proposed a task-driven Generative Adversarial Network (GAN) model for retinal vessel segmentation, showcasing significant improvements in accuracy, sensitivity, specificity, and Area Under the Curve (AUC) compared to traditional methods. However, their exclusion of Transformer-based architectures and attention mechanisms as segmentation backbones limited the potential for leveraging enhanced feature representation and context integration, which could have further enhanced diagnostic capabilities. Furthermore, Abdulsahib et al. [14] proposed the introduction of a fully automatic blood vessel segmentation algorithm for retinal fundus images promised improved diagnostic precision and reduced workload for ophthalmologists.

Despite exceptional performance on challenging datasets like DRIVE and HRF, the absence of exploration into Transformer-based architectures and attention mechanisms for segmentation highlighted a potential limitation in harnessing the latest advancements in deep learning for optimal segmentation outcomes. In summary, while these studies represented significant strides in leveraging deep learning for ophthalmological applications, the limited exploration of advanced XAI techniques and cutting-edge architectural methodologies presented a notable gap in maximizing the potential of these approaches for enhanced interpretability, transparency, and diagnostic accuracy.

Within the scope of our research, we introduce two distinct pipelines that improve the understanding and interpretation of fundus images. The first pipeline is primarily concerned with classifying these images. We accomplish this by combining five different XAI techniques and utilizing the capabilities of eight different CNNs. This combination aims to quickly categorize images while simultaneously attempting to offer understandable explanations for the classifications that are constructed. We explore the complex field of retinal blood vessel segmentation with Attention U-Net variations, Trans U-Net variations, Swin-UNET, in our second pipeline. This stage contributes to a more thorough knowledge of the vascular system by carefully examining and precisely separating the complex network of blood vessels within the fundus images.

Our research focuses on a comprehensive evaluation of two pivotal pipelines for fundus image processing, aiming to discern their strengths and weaknesses. By rigorously assessing their performance, we aspire to propel the field of fundus image analysis forward significantly. Through meticulous exploration of diverse methodologies, our study seeks to enrich the ongoing discourse and understanding in medical imaging. Ultimately, we aim to deepen insights into fundus image analysis, offering valuable contributions to healthcare and diagnostic imaging industries.

Our paper makes significant contributions in several key areas:

- We conducted a comprehensive comparison of the performance of eight widely-used pre-trained CNN models, namely ResNet101, DenseNet169, Xception, InceptionV3, DenseNet121, InceptionResNetV2, ResNet50, and EfficientNetB0.
- To enhance the interpretability of our pre-trained CNN models, we employed Explainable AI techniques such as Grad-CAM, Grad-CAM++, Score-CAM, Faster Score-CAM, and Layer CAM. These techniques help shed light on the rationale behind the models' predictions, contributing to a deeper understanding of their decision-making processes.
- We explore Attention U-Net models, which have a variety of architectures and use reputable backbones including DenseNet201, DenseNet169, DenseNet121, ResNet50V2, ResNet101V2, and ResNet152V2. We also explore novel techniques such as TransUNet, combining backbones like ResNet50V2, ResNet101V2, and ResNet152V2, and examining architectures like the Swin-Unet.
- For fundus image classification, we employed a set of diverse evaluation metrics, including Accuracy, Precision, Recall, F1 Score, Jaccard Score, and Log Loss. In the context of segmentation, we utilized Intersection over Union (IoU), Dice Coefficient, Mean Pixel Accuracy, Mean Modified Hausdorff Distance, and Mean Surface Dice Overlap.

The remaining part of the paper is structured as follows:

The subsequent sections of the paper are organized as follows: Section 2 presents a comprehensive review of relevant literature, laying the groundwork for our research. Section 3 provides an overview of the datasets employed in the study, while Section 4 delves into background studies on Gradient-based Explainable AI, Pre-trained Convolutional Neural Networks, and Segmentation Models. Section 5 addresses evaluation metrics for both classification and segmentation tasks, followed by Section 6, which outlines the suggested strategy and analytical steps. Section 7 details the experimental setup and hyper-parameter settings, while Section 8 discusses the interpretation of results. Section 9 further explores findings, analyzing methods of Explainable AI and conducting a comparative performance analysis. Section 10 addresses limited areas of investigation, while Section 11 suggests potential avenues for further exploration. Finally, Section 12 summarizes the study’s key findings and their significance for Retinal Fundus Classification and Retinal Blood Vessel Segmentation Techniques in the realm of medical imaging.

2 Related Works

2.1 Retinal Fundus Classification without using XAI Techniques

Muhammad et al. [15] classified Fundus Image Classification Using VGG-19 Architecture with principle component analysis (PCA) and singular value decomposition (SVD). A standard KAGGLE dataset including 35,126 images was used for the experiments. The application of fully connected (FC) layers in PCA and SVD feature selection obtained 92.21%, 98.34%, 97.96% and 98.13% classification accuracies for FC7-PCA, FC7-SVD, FC8-PCA and FC8-SVD respectively. In another research, Al-Omaisi et al. [16] detected Diabetic Retinopathy in Retinal Fundus Images Using CNN Classification Models. The images dataset in this study is obtained from XHO which consists of 1607 images. They achieved test accuracy of 98.82% with ResNet-101, 91.50% with ResNet-50, and 64.11% with VggNet-16. The work of Yuhang et al. [17] developed an automated deep learning system to classify fundus images into three distinct categories: tessellated fundus, normal and macular degeneration. Using a fundus camera, a total of 1,032 fundus images were obtained from 516 patients. The fundus images were then classified using Inception V3 and ResNet-50 deep learning models. Using ResNet-50 and Inception V3, they obtained the highest accuracy of 93.81% and 91.76% respectively. This system will help in the early detection and management of many diseases, including diabetic retinopathy. Also Rohit et al. [18] proposed a sophisticated computer-assisted triage system that uses machine learning and deep neural networks to create and evaluate color retinal fundus pictures and categorize retinal images of glaucoma patients. The suggested approach examined and evaluated all images from public datasets like ORIGA and DRISTHI-GS1. Logistic Regression based machine learning-based classifier outperforms all other six different classifiers in the experiment. Logistic regression-based machine learning classifier outperforms all six other classifiers in the experiment.

2.2 Retinal Fundus Classification using XAI Techniques

Yeonwoo et al. [1] classified laterality of fundus images using interpretable Deep Neural Network. 25,911 fundus images were used to test and train their model. Their suggested model outperforms VGG-16 and performs comparably to AlexNet, with an accuracy of mean 98.9% with standard variation of 0.11% in all type of images. Yusaku et al. [19] classified fundus images by their severity index and the recognition accuracies for Japanese and American data were compared. 35,126 fundus images from an American hospital and 200 fundus images from a Japanese hospital, respectively; the two datasets named EyePACS and KEIO were used in the study. They trained a deep convolutional neural network and a support vector machine on these dataset. The trained artificial intelligence model showed an 81.5% sensitivity and a 71.9% specificity for the EyePACS dataset, as well as a 90.8% sensitivity and an 80.0% specificity for the Keio dataset. Conversely, Kyoung et al. [8] used 628 fundus images to develop an AI model that was classified using three convolutional neural network architectures—ResNet50, VGG19, and Inception v3. In predicting the diagnosis of nine categories, which included eight retinal diseases and normal cases, the ResNet50 model outperformed with an accuracy of 87.42%. On the contrary, Gongpeng et al. [20] evaluated a deep learning model based on ultra-widefield images (UWFIs) that can detect several common fundus diseases. The model was tested on three test sets with data volumes of 465, 979, and 525. The performance of the three deep learning networks, EfficientNet-B7, DenseNet, and ResNet-101, was evaluated on the internal test set. Compared to the other two deep learning models, EfficientNet-B7 achieved the best performance.

2.3 Retinal Blood Vessel Segmentation Techniques

Wenjing et al. [21] offers a novel retinal vessel segmentation method using the B-COSFIRE filter for diagnosing diabetic retinopathy and glaucoma. By integrating contrast enhancement, region of interest extraction, and morphological filtering, it achieves accurate results with minimal processing time. Evaluations on DRIVE, STARE, and CHASEDB1 datasets show competitive performance metrics, making it suitable for real-time diagnosis. Yun et al. [22] discloses an innovative technique for segmenting retinal fundus images, vital for detecting diabetic-induced eye diseases early. It merges U-Net architecture with recurrent neural networks to precisely delineate optic disc, optic cup, and retinal blood vessels. With its cutting-edge performance, the model offers significant potential to enhance the diagnosis and treatment of diabetic-related eye conditions, ultimately mitigating irreversible blindness risks. Pengshuai et al. [23] introduces a novel deep guidance network tailored for biomedical image segmentation tasks, particularly focusing on retinal vessel and optic disc segmentation in fundus images. By integrating a guided image filter module, the network effectively restores spatial information lost during down-sampling operations, improving accuracy and edge preservation. The proposed method enables end-to-end training and fast inference, with extensive experiments conducted on four publicly available datasets to validate its effectiveness. Compared to traditional approaches and popular architectures like U-Net, the proposed network showcases promising

Table 1: Overview of Key Findings in Retinal Fundus Classification using XAI Techniques and without using XAI Techniques

Types	Authors	Publication Year	Models Employed	Performance Assessment
Classification without XAI	Muhammad et al. [15]	2018	VGG19	Accuracy 92.21%
	Al-Omais et al. [16]	2022	ResNet-101, ResNet-50, VggNet-16	Accuracy: ResNet-101: 98.82% , ResNet-50: 91.5% and VggNet-16: 64.11%
	Yuhang et al. [17]	2023	InceptionV3 and ResNet-50	Accuracy: ResNet-50: 93.81% InceptionV3: 91.76%
	Rohit et al. [18]	2023	Proposed model	Accuracy: DRISTHI-GS 99%, ORIGA 99.4%
Classification with XAI	Yeonwoo et al. [1]	2018	Proposed CNN model	Accuracy: 98.9%
	Yusaku et al. [19]	2020	SVM and NN classifiers	sensitivity: 81.5%, Specificity: 71.9%
	Kyoung et al. [8]	2021	VGG19, Inceptionv3, ResNet50	Accuracy: VGG19:82%, Inceptionv3: 83.40%, ResNet50: 87.40%
	Gongpeng et al. [20]	2022	EfficientNet-B7, DenseNet, and ResNet-101	Average AUC: EfficientNet-B7: 0.9880, ResNet-101: 0.9784, and DenseNet: 0.9830

results, offering a simple yet efficient solution for accurate biomedical image segmentation, crucial for diagnostic applications in ophthalmology. Zhiyuan et al. [13] unveils a novel retinal vessel segmentation method using a task-driven generative adversarial network (GAN). Leveraging a U-Net generative model and multi-scale discriminators, the approach achieves significant improvements in accuracy, sensitivity, specificity, and area under the ROC curve compared to traditional methods. By integrating perceptual loss for task-specific image generation, the proposed method demonstrates promising potential for automated retinal vessel segmentation, offering

valuable contributions to medical imaging and diagnosis. S. Alex et al. [24] presents an enhanced U-Net architecture for segmenting retinal blood vessels in fundus images. By incorporating multiscale inputs and dense blocks, the proposed method achieves improved accuracy, sensitivity, and specificity compared to traditional U-Net models. It addresses challenges in segmenting thin vessels and demonstrates promising results in detecting glaucoma-related changes in the optic disc. The proposed approach offers a cost-effective and efficient solution for early diagnosis of eye disorders using fundus images. Changlu et al. [25] introduces SA-UNet, a novel deep learning network designed for the precise segmentation of retinal blood vessels. SA-UNet addresses the challenges of limited annotated data and potential overfitting by incorporating a spatial attention module and structured dropout convolutional blocks. The spatial attention mechanism enhances feature refinement, while dropout blocks prevent overfitting. Experimental results on benchmark datasets demonstrate that SA-UNet achieves state-of-the-art performance in retinal vessel segmentation, making it a promising tool for medical image analysis in ophthalmology. Manizheh et al. [26] provides a novel approach for the segmentation of retinal blood vessels using the U-Net++ architecture and subsequent disease prediction based on retinal images. By employing a multi-stage method that includes color image enhancement, Gabor filter application, and feature extraction using HOG and LBP, the proposed method achieves high accuracy in segmenting retinal images and diagnosing diseases such as diabetic retinopathy. The results demonstrate superior performance compared to previous methods, showcasing the effectiveness of the proposed approach in medical image analysis and diagnosis. Ko-Wei et al. [27] introduces a novel approach for retinal vessel segmentation in medical images using an enhanced U-Net model. By incorporating residual modules and full-scale skip connections, the proposed method effectively integrates low-level and high-level features for accurate segmentation. It outperforms existing models like U-Net 3+, ResUNet, and ResUNet++ on benchmark datasets.

3 Dataset Description

For classification purposes, the FIVES [28] Database was employed, while for segmentation tasks, two databases were utilized: DRIVE [29] and FIVES [28]. Table 3 provides an overview of the FIVES and DRIVE datasets, detailing their descriptions, sizes, resolutions, and the tasks they were utilized for in the study.

3.1 FIVES

The Fundus Image Vessel Segmentation (FIVES) [28] collection consists of 800 color fundus photos with high resolution. Images were saved with a resolution of 2048×2048 pixels in PNG format. During the procedures of taking pictures, annotating them, and submitting datasets, no image compression was done. Three labels are provided for each image by medical staff crowdsourcing the annotation process: disease categorization, pixel-by-pixel vascular annotation, and quality of image scores. Three distinct

Table 2: Overview of Key Findings in Retinal Blood Vessel Segmentation Techniques

Types	Authors	Publication Year	Models Employed	Performance Assessment
Segmentation	Ko-Wei et al. [27]	2023	U-net, U-Net 3+, ResUNet, ResUNet++	DRIVE dataset IOU: 60.8, Rose dataset: IOU: 59.3
	Wenjing et al. [21]	2022	B-Cosfire filter, Morphologic filter	DRIVE Sensitivity: 0.7339, Specificity: 0.9847, Accuracy: 0.9604
	Manizheh et al. [26]	2022	U-Net++	Accuracy: 0.989, Sensitivity: 0.941, Specificity: 0.988
	S. Alex et al. [24]	2022	U-Net Vanilla U-Net	Vanilla U-net: ACC: 0.9557, Sen: 0.712, Spec: 0.992
	Yun et al. [22]	2020	U-Net, RU-Net, R2U-Net	Optic Cup Segmentation: Accuracy: 0.9950, Dice coefficient: 0.8921
	PENGSHUAI et al. [23]	2020	U-net, DU-net, LaderNet, CE-Net	Accuracy: 0.9709, Sensitivity: 0.8510, Specificity: 0.9916
	Zhiyuan et al. [13]	2020	U-Net	Accuracy: 0.9683, Sensitivity: 0.8066, Specificity: 0.9897
	Changlu et al. [25]	2020	U-net, U-net+SA, SD-Unet, SA-Unet	Accuracy:0.9698, AUC: 0.9864, F1: 0.8263

eye illnesses and 200 photos of healthy eyes are included in the dataset. An annotation entails pixel-by-pixel labeling by a team of medical professionals with training, confirmed by expert ophthalmologists. The FIVES dataset is anticipated to have a substantial impact on machine learning retinal vascular segmentation research as well as the advancement of technology towards therapies. Sample images from this dataset appear in Figure 1.

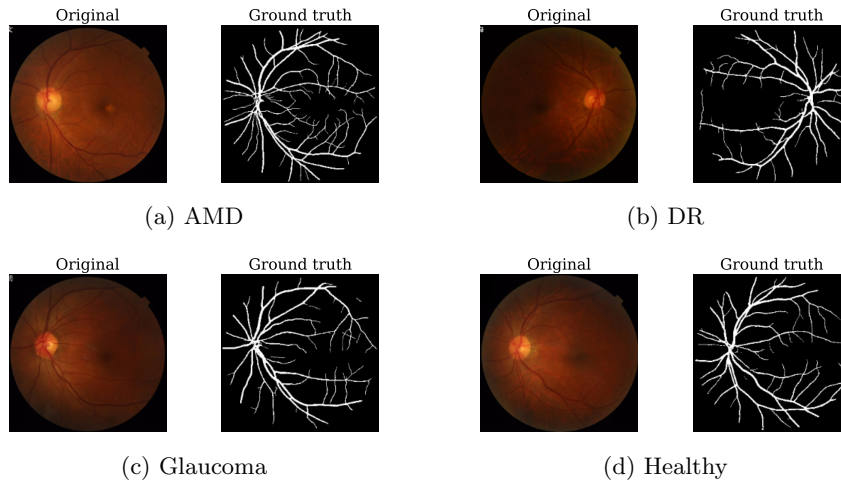


Fig. 1: Some instances of Fundus Image Vessel Segmentation (FIVES) Dataset

Table 3: Overview of the Datasets

Dataset Name	Description	Total Images	Resolution	Task Applied
FIVES	200 healthy, 600 diseases Images (glaucoma, DR, and AMD).	800	2048 × 2048	Classification Segmentation
DRIVE	33 healthy, 7 diseases Images.	40	768 × 584	Segmentation

3.2 DRIVE

The Digital Retinal Images for Vessel Extraction (DRIVE) [29] dataset includes 40 JPEG color fundus images designed for retinal vessel segmentation. These images were sourced from a screening program for diabetic retinopathy in the Netherlands, using a Canon CR5 camera with a 45-degree field of view. A subset of 40 images was randomly selected from 400 diabetes subjects aged 25 to 90 who underwent screening. Each image, measuring 584×565 pixels with eight bits per color channel, contains 7 abnormal cases and is divided into training and testing sets, each comprising 20 images. The dataset encompasses circular field of view masks and manual segmentations conducted by ophthalmologist. It serves as a standardized benchmark for evaluating retinal vessel segmentation methods, contributing to the diagnosis of cardiovascular and ocular diseases in diabetic individuals. Few Sample images from this dataset appear in Figure 2.

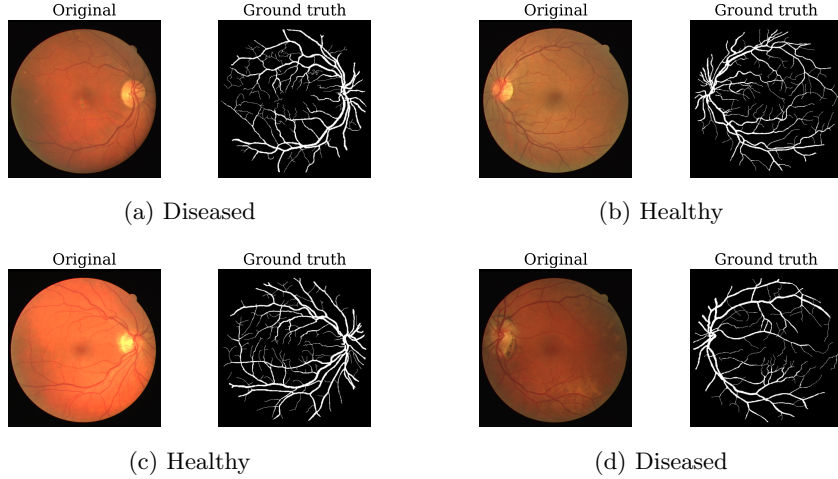


Fig. 2: Some instances of The Digital Retinal Images for Vessel Extraction (DRIVE) Dataset

4 Background Study

4.1 Gradient-based Explainable AI

4.1.1 Grad-CAM:

Grad-CAM [30], or Gradient-weighted Class Activation Mapping, is a technique used in deep learning for visualizing the significant regions of an input image that contribute to a specific class prediction in CNNs. During the forward pass, it computes the gradients of the predicted class score with respect to the feature maps, indicating their sensitivity. These gradients are then weighted based on the global average pooling (GAP) of the gradients for each feature map, generating a weighted sum. The resulting weighted sum is passed through a ReLU activation to create an activation map, highlighting the influential regions of the input image for the predicted class. Grad-CAM provides valuable interpretability by offering a visual representation of the areas crucial for a CNN’s decision-making process, aiding in understanding and validating the network’s behavior. The formula for Grad-CAM can be stated as follows:

$$\alpha_k^c = \frac{1}{Z} \sum_i \sum_j \frac{\partial Y^c}{\partial A_{ij}^k} \quad (1)$$

This equation has the following components:

- α_k^c represents the importance of the feature map k for class c .
- Z is the normalization factor, often the number of elements in the feature map.
- Y^c is the class score before the softmax activation.
- A_{ij}^k represents the activation of the k th feature map at spatial location (i, j) .

4.1.2 Grad-CAM++:

Grad-CAM++ (Gradient-weighted Class Activation Mapping++) [31] extends the Grad-CAM method, providing a means to visualize and comprehend the influential regions within an input image for a CNN prediction. By introducing second-order derivatives, Grad-CAM++ refines interpretability, enhancing accuracy in localizing critical areas. The method begins with a forward pass, where the input image traverses the CNN, yielding final convolutional feature maps that capture channel activations. Gradients of the predicted class score are then computed, elucidating the impact of each feature map on the score. Employing Global Average Pooling on these gradients produces importance weights for each feature map, reducing dimensionality to a single weight per channel. Second-order gradients, calculated through backpropagation, provide additional information about the channels. The ultimate visualization is derived by a weighted sum of feature maps, combining first-order and second-order gradients, delivering a nuanced depiction of the image regions influencing the CNN’s decision-making process. The equation for Grad-CAM++ is expressed as follows:

$$\alpha_k^c = \frac{1}{Z} \sum_i \sum_j \frac{\partial^2 Y^c}{\partial A_{ij}^k \partial A_{ij}^k} + \frac{2}{Z} \sum_i \sum_j \frac{\partial Y^c}{\partial A_{ij}^k} \quad (2)$$

This equation includes the following elements:

- α_k^c represents the importance of the feature map k for class c .
- Z is the normalization factor, often the number of elements in the feature map.
- Y^c is the class score before the softmax activation.
- A_{ij}^k represents the activation of the k th feature map at spatial location (i, j) .
- The first term represents the second-order derivatives, and the second term represents the first-order derivatives.

4.1.3 Score-CAM:

Score-CAM (Score-weighted Class Activation Mapping) [32] is a technique designed for elucidating the pivotal regions within an input image that significantly influence a neural network’s classification output. Tailored for classification tasks, Score-CAM enhances interpretability by incorporating class-specific information. In the method’s forward pass, the input image undergoes processing through the neural network, yielding final convolutional feature maps. Class Activation Maps (CAM) are then computed via global average pooling on these feature maps, highlighting spatial locations crucial to the class score. Subsequently, class scores are generated by linearly combining CAM values with weights learned from the fully connected layer. Gradients of the class score with respect to the feature maps are calculated, guiding the determination of weights. The final visualization is derived by a weighted sum of feature maps, utilizing these computed gradients as weights, providing a refined and localized interpretation of the neural network’s predictions in the context of classification tasks such as Retina Fundus Image Classification. The mathematical expression for Score-CAM is represented as:

$$\alpha_k^c = \frac{1}{Z} \sum_i \sum_j \frac{\partial Y^c}{\partial A_{ij}^k} \quad (3)$$

This equation contains:

- α_k^c represents the importance of the feature map k for class c .
- Z is the normalization factor, often the number of elements in the feature map.
- Y^c is the class score before the softmax activation.
- A_{ij}^k represents the activation of the k th feature map at spatial location (i, j) .

4.1.4 Faster Score-CAM:

Faster Score-CAM [33] for Retina Fundus Image Classification is an optimization technique aimed at enhancing the efficiency of interpreting CNNs in the context of classifying retinal fundus images. Traditional Score-CAM calculates weights for all channels in a chosen feature map, which can be computationally expensive. In response, Faster Score-CAM focuses on channels with high variance, assuming they contain more discriminative information. The process involves calculating mean and variance for each channel, selecting the top N channels with the highest variance, and then using these channels to compute weights and generate a heatmap. The benefits include faster computation, making it more practical for analyzing large datasets of retinal fundus images, while still providing valuable insights into influential image regions for classification tasks like diabetic retinopathy or glaucoma. However, choosing the optimal value for N involves a trade-off between speed and capturing informative details in the heatmap, requiring careful experimentation. The mathematical formulation for Faster Score-CAM is provided as:

$$\alpha_k = \frac{\text{Var}(A_k)}{\sum_{j=1}^N \text{Var}(A_j)} \quad (4)$$

Within the following formula:

- α_k represents the weight assigned to channel k .
- $\text{Var}(A_k)$ is the variance of activations in channel k .
- N is the total number of channels in the chosen feature map.

4.1.5 Layer CAM:

Layer-CAM [34] is an insightful visualization technique that enhances our understanding of a CNN decision-making process in the realm of retinal fundus image classification. Operating on the final convolutional layer just before the classification layer, Layer-CAM identifies and highlights critical regions within an image that contribute significantly to a specific class prediction. What sets Layer-CAM apart is its capacity to generate reliable class activation maps not only from the final convolutional layer but also from shallow layers, allowing for a balance between coarse spatial locations and fine-grained object details. By considering the entire convolutional layer, Layer-CAM calculates weights for each channel based on their impact on the class score, creating a heatmap that visually represents the network’s attention during classification. Importantly, Layer-CAM’s ability to produce class activation maps from different layers, each offering complementary insights, allows for the generation of more precise and integral class-specific object regions. The ease of application

to off-the-shelf CNN-based image classifiers, without altering network architectures or back-propagation methods, adds to Layer-CAM’s convenience and broad applicability, making it a valuable tool for various image analysis tasks. The mathematical representation of Layer-CAM is as follows:

$$S_c(x) = \text{ReLU} \left(\sum_{c=1}^C (W_c \times \text{Score}(c, F(x))) \right) \quad (5)$$

This equation contains the following components:

- $F(x)$ - Output of the final convolutional layer for an input image x . This is a 3D tensor with dimensions (H, W, C) , where H and W are the height and width of the feature map, and C is the number of channels.
- W_c - Weight for channel c in the convolutional layer.
- $\text{Score}(c, F(x))$ - Function that computes the contribution of channel c to the class score for a particular class. This can be a simple linear function or a more complex function depending on the model architecture.
- $S_c(x)$ - Class activation map for class c .

4.2 Pre-trained Convolutional Neural Networks

4.2.1 ResNet101:

ResNet101 [35], a key member of Residual Networks (ResNets), tackles the challenge of training deep neural networks by introducing residual learning. It uses skip connections to smooth gradient flow during backpropagation. With 101 layers, its architecture comprises residual blocks containing multiple convolutional layers and shortcut connections, which can perform identity mapping or involve a 1x1 convolution for dimension matching. Employing a bottleneck architecture in its residual blocks, ResNet101 combines 1x1, 3x3, and 1x1 convolutions to reduce computational complexity while maintaining expressive power, effectively capturing complex features.

4.2.2 DenseNet169:

DenseNet169 [36] is a convolutional neural network belonging to DenseNets, designed to overcome challenges in deep networks. It features dense connectivity, where every layer connects to every other layer, promoting direct information flow and enhancing gradient flow during training. The architecture incorporates bottleneck layers within dense blocks, reducing computational complexity while maintaining feature richness. Dense connectivity fosters efficient feature reuse, aiding in meaningful hierarchical feature extraction. Transition blocks control network growth and spatial dimensions.

4.2.3 Xception:

Xception [37] is a Google-developed convolutional neural network architecture, notable for its extreme inception-style design. The name “Xception” merges “Extreme” and “Inception,” signifying its innovative approach. Noteworthy features include extreme depth-wise separable convolutions, replacing traditional convolutions for heightened

computational efficiency. Drawing inspiration from the Inception architecture, Xception employs depth-wise separable convolutions in multiple parallel paths, reducing parameters and computation. A distinctive global depth-wise separable convolution captures global dependencies, efficiently merging spatial and channel-wise information, thereby enhancing the model’s representational capabilities.

4.2.4 InceptionV3:

InceptionV3 [38], part of Google’s Inception family, is a CNN architecture celebrated for its efficiency in image classification and computer vision tasks. Key features include the incorporation of the inception module, utilizing parallel convolutional operations with diverse filter sizes (1x1, 3x3, 5x5) and max-pooling to capture multi-scale features and hierarchical representations. To enhance computational efficiency, InceptionV3 employs factorization techniques, breaking down larger convolutions while maintaining pattern capture. The introduction of auxiliary classifiers at intermediate layers aids in addressing the vanishing gradient problem and provides regularization, enhancing overall training and generalization.

4.2.5 DenseNet121:

DenseNet121 [39] is a convolutional neural network renowned for its dense connectivity pattern, fostering feature reuse and propagation throughout the network. It consists of 121 layers organized into dense blocks, transition layers, and a final global average pooling layer followed by a softmax classifier. Dense blocks contain densely connected convolutional layers, while transition layers control spatial dimensions and feature map numbers between dense blocks, often involving batch normalization, 1x1 convolutions, and average pooling for dimensionality reduction and downsampling.

4.2.6 InceptionResNetV2:

InceptionResNetV2 [40], a robust CNN architecture introduced by Google, seamlessly blends features from Inception and ResNet models. Leveraging the inception module akin to InceptionV3, it employs parallel convolutional operations with diverse filter sizes and max-pooling, facilitating the capture of multi-scale features and hierarchical representations. Integrating residual connections inspired by ResNet, InceptionResNetV2 enables direct information flow between layers, addressing the vanishing gradient problem for effective training of deep networks. The inclusion of bottleneck layers, combining 1x1 and 3x3 convolutions, optimizes computational complexity while preserving expressive power. Further, the architecture incorporates reduction blocks and auxiliary classifiers to downsample spatial dimensions and enhance training robustness, respectively.

4.2.7 ResNet50:

ResNet50 [41], part of the ResNet family developed by Microsoft Research, stands out for its effectiveness in training deep neural networks by addressing the vanishing gradient problem. It introduces the concept of residual learning, employing short-cut connections to enable a direct information flow between layers. The bottleneck

architecture within its residual blocks, incorporating 1x1, 3x3, and 1x1 convolutions, efficiently reduces computational complexity while preserving expressive power. The “50” signifies the total number of layers, reflecting a balanced architecture that achieves sufficient depth for capturing intricate features without becoming overly computationally demanding.

4.2.8 EfficientNetB0:

EfficientNetB0 [42], part of the EfficientNet family, is known for its balanced accuracy and computational efficiency achieved through compound scaling. It uniformly scales depth, width, and resolution, ensuring increased capacity without a significant rise in computational demands. By employing depth-wise separable convolutions, it efficiently splits spatial and channel-wise correlations, reducing parameters and computational costs while maintaining expressive power. The integration of bottleneck blocks, combining 1x1 and 3x3 convolutions, optimizes the trade-off between computational efficiency and feature representation.

4.3 Segmentation Models

4.3.1 TransUNet:

TransUNet [43] stands out as a powerful solution for medical image segmentation, seamlessly integrating the advantages of both U-Net and Transformers. The framework introduces self-attention mechanisms to address feature resolution loss in Transformers, employing a hybrid CNN-Transformer architecture. By harmonizing detailed spatial information from CNN features with the global context encoded by Transformers, TransUNet tactically upsamples and combines features, ensuring precise localization within a u-shaped design. Empirical evidence underscores TransUNet’s superior performance across diverse medical image segmentation tasks, showcasing the efficacy of our Transformer-based approach. This innovative framework highlights the significance of incorporating low-level features for heightened segmentation accuracy, offering a promising avenue for advanced medical imaging applications.

4.3.2 Attention U-Net:

The Attention U-Net [44] represents an advancement in medical image segmentation over the standard U-Net model. Through the incorporation of attention gates (AG), this architecture excels by autonomously prioritizing target structures of diverse shapes and sizes. The AGs effectively eliminate the reliance on explicit external localization modules, streamlining the network. This enhancement, seamlessly integrated into the U-Net framework with minimal computational overhead, heightens model sensitivity and prediction accuracy. Notably, the attention mechanism surpasses previous approaches by introducing grid-based gating, offering improved specificity to local regions. The utilization of a soft-attention technique in a feed-forward CNN for medical imaging is a pioneering feature, replacing hard-attention methods in image classification and external organ localization models.

4.3.3 Swin-UNET:

Swin-Unet [45] is a specialized deep learning model tailored for medical image segmentation, diverging from conventional U-Net architectures by integrating the Swin Transformer. Inspired by U-Net, it retains the U-shaped encoder-decoder design with skip connections for holistic information capture. The Swin Transformer in the encoder offers efficiency in processing high-resolution images through parallelized patch-based handling, while excelling at capturing long-range dependencies crucial for understanding intricate medical structures. The decoder, also employing a Swin Transformer, incorporates a “patch expanding layer” for resolution enhancement during upsampling, aiding in the recovery of spatial details lost in the encoding phase. The use of skip connections ensures direct injection of high-resolution feature maps into the decoder, preserving vital spatial information. Swin-Unet emerges as a potent alternative for medical image segmentation, leveraging the advantages of Swin Transformers for efficient and contextually rich analysis of complex medical data.

5 Evaluation metrics for both Classification and Segmentation

5.1 Classification Metrics

5.1.1 Accuracy:

Accuracy [46] is a vital metric in Fundus Image Classification as it encapsulates the overall correctness of the model in accurately categorizing fundus images. It serves as a comprehensive gauge of the model’s effectiveness in handling various cases. The score can be calculated as:

$$Accuracy = \frac{\text{Number of Correctly Classified Fundus Images}}{\text{Total Number of Fundus Images}} \quad (6)$$

5.1.2 Precision:

Precision [46] is crucial in Fundus Image Classification, emphasizing the model’s accuracy in identifying positive cases, such as detecting eye diseases in fundus images. It aims to minimize false positives, enhancing the model’s reliability by avoiding unnecessary alarms for healthy conditions. Precision is calculated as follows:

$$Precision = \frac{\text{Correctly Classified Fundus Images}}{\text{Total Classified Fundus Images}} \quad (7)$$

5.1.3 Recall:

Recall [46], also known as Sensitivity or True Positive Rate, is vital in Fundus Image Classification, assessing the model’s capability to capture all actual positive instances. It prevents overlooking potential cases of eye diseases in fundus images, emphasizing comprehensive detection. The formula for recall is as follows:

$$\text{Recall} = \frac{\text{Correctly Classified Fundus Images}}{\text{Total Actual Fundus Images}} \quad (8)$$

5.1.4 F1 Score:

The F1 Score [46] is a crucial metric in Fundus Image Classification, effectively balancing precision and recall. By offering a harmonic mean, it provides a comprehensive evaluation of the model's performance in detecting eye diseases in fundus images. This balance ensures accurate identification of positive cases while capturing all instances, contributing to a robust and reliable classification system. The formula for the F1 Score is:

$$\text{F1 Score} = \frac{2 \cdot \text{Precision for Fundus Images} \cdot \text{Recall for Fundus Images}}{\text{Precision for Fundus Images} + \text{Recall for Fundus Images}} \quad (9)$$

5.1.5 Jaccard Score:

Jaccard Score [47], also known as Intersection over Union, is important in Fundus Image Classification for measuring the similarity between predicted and actual positive instances within images. Jaccard Score is calculated using the following formula:

$$\text{Jaccard Score} = \frac{\text{Union Area of Predicted Images and Actual Images}}{\text{Intersection Area of Predicted Images and Actual Images}} \quad (10)$$

5.1.6 Log Loss:

The computation of Log Loss [46], also known as Logarithmic Loss, is essential to Fundus Image Classification since it evaluates the model's prediction confidence by taking into account probability values for different classes. For Log Loss, the following formula applies:

$$\text{Log Loss} = -\frac{1}{N} \sum_{i=1}^N \sum_{j=1}^C y_{ij} \log(p_{ij}) \quad (11)$$

where:

- N is the total number of fundus images,
- C is the total number of classes (e.g., normal, diabetic retinopathy, glaucoma, etc.),
- y_{ij} is a binary indicator of whether fundus image i belongs to class j ,
- p_{ij} is the predicted probability that fundus image i belongs to class j .

5.2 Segmentation Metrics

5.2.1 Intersection over Union (IoU):

IoU [48] measures the overlap between the predicted and ground truth segmentation masks. Specifically, in retinal blood vessel segmentation, IoU quantifies the agreement between the segmented vessels and the actual vessel locations. It is a valuable metric for assessing the spatial accuracy of the segmentation model. The Intersection over Union (IoU) is defined as:

$$IoU = \frac{\textit{Area of Intersection}}{\textit{Area of Union}} \quad (12)$$

5.2.2 Dice Coefficient:

Similar to IoU, the Dice Coefficient [49] evaluates the overlap between predicted and ground truth segmentations. It is particularly useful in the context of retinal blood vessel segmentation as it provides a balanced measure of segmentation accuracy, emphasizing both false positives and false negatives. It is calculated as twice the intersection divided by the sum of areas of the predicted and ground truth masks. The equation for the dice coefficient is as follows:

$$Dice = \frac{2 \times |A \cap B|}{|A| + |B|} \quad (13)$$

Where:

- A represents the predicted segmentation mask,
- B represents the ground truth segmentation mask.

5.2.3 Mean Pixel Accuracy:

Mean Pixel Accuracy [50] assesses the accuracy of individual pixel-wise classifications in the segmented images. In retinal blood vessel segmentation, this metric measures the overall correctness at the pixel level, offering insights into the model's ability to precisely delineate vessel boundaries. The following formula yields the mean pixel accuracy:

$$\textit{Mean Pixel Accuracy} = \frac{\textit{Number of correctly classified pixels}}{\textit{Total number of pixels}} \quad (14)$$

5.2.4 Mean Modified Hausdorff Distance:

Mean Modified Hausdorff Distance [51] quantifies the dissimilarity between the predicted and ground truth segmentation masks, emphasizing the spatial discrepancies. In retinal blood vessel segmentation, this metric helps evaluate how well the model captures the overall structure and spatial distribution of blood vessels. The equation for the Mean Modified Hausdorff Distance is as follows:

$$\text{Mean Modified Hausdorff Distance} = \frac{1}{N} \sum_{i=1}^N \frac{1}{|B|} \sum_{b \in B} \min_{a \in A} d(a, b) \quad (15)$$

where:

- N is the total number of ground truth segmentation masks,
- A represents the predicted segmentation mask,
- B represents the ground truth segmentation mask,
- $d(a, b)$ denotes the distance between pixel a in the predicted mask and pixel b in the ground truth mask.

5.2.5 Mean Surface Dice Overlap:

Mean Surface Dice Overlap [52] assesses the agreement between the predicted and ground truth surfaces, providing a comprehensive measure of segmentation accuracy. In retinal blood vessel segmentation, it is particularly valuable for evaluating how well the model captures the 3D structure and complexity of blood vessels. Below is the equation for the Mean Surface Dice Overlap:

$$\text{Mean Surface Dice Overlap} = \frac{1}{N} \sum_{i=1}^N \frac{2 \times |A_i \cap B_i|}{|A_i| + |B_i|} \quad (16)$$

where:

- N is the total number of samples or images,
- A_i represents the predicted surface for the i -th sample,
- B_i represents the ground truth surface for the i -th sample.

6 Suggested Approach

We advance the area of retinal image analysis with our suggested strategy, which includes two essential pipelines. Accurately classifying retinal fundus images into different disease groups is the aim of Pipeline 1’s Retina Fundus Classification. A crucial step in medical image processing for the diagnosis of retinal disorders, Pipeline 2 explores Retinal Blood Vessel Segmentation. Prepare the dataset, choose a model, train, interpret, and evaluate it all with care using one of two workflows. We want to improve the accuracy and interpretability of retinal image analysis systems by utilizing cutting-edge methods and models by employing this methodical strategy. Figure 3 demonstrate progressing Retinal Image Analysis by using two pipelines for Classifying Retinal Fundus and Segmenting Retinal Blood Vessels.

6.1 Pipeline 1: Retina Fundus Classification

1) Dataset Preparation: In this critical phase, our focus was on meticulously assembling a diverse dataset of retinal fundus images, laying the foundation for robust model training. The dataset we employed comprises a rich variety of images capturing different aspects of retinal conditions from the FIVES dataset. The images

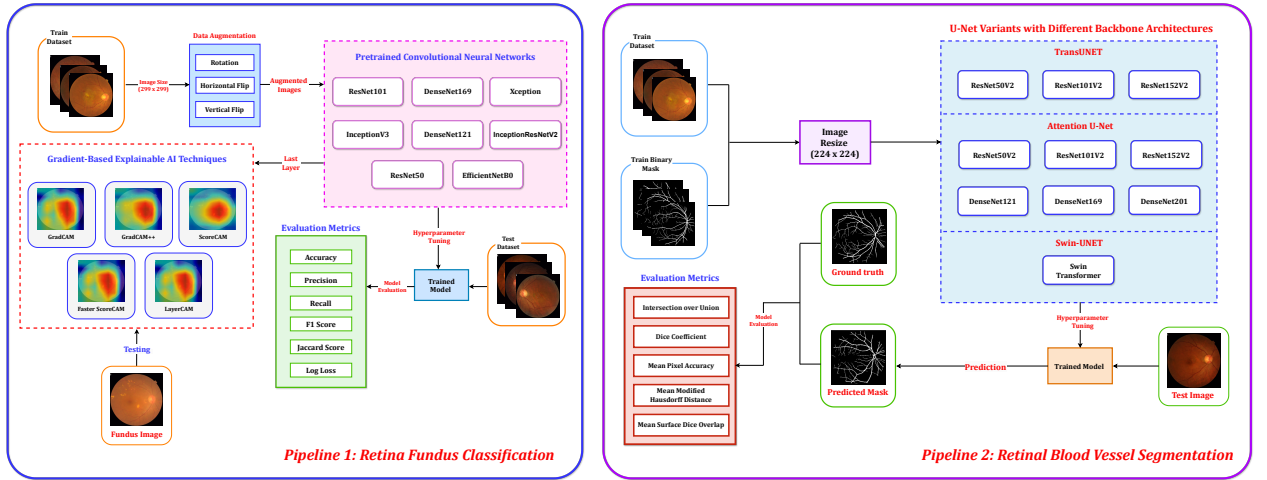


Fig. 3: Progressing Retinal Image Analysis by Using Two Essential Pipelines for Classifying Retinal Fundus and Segmenting Retinal Blood Vessels

are carefully curated to ensure representation across various demographics and pathological conditions. To ensure seamless compatibility with our chosen pre-trained CNN models, we meticulously tailored our dataset by adopting specific image dimensions. Images were uniformly resized to 299 x 299 pixels, optimizing them for efficient processing. To enhance the model’s ability to generalize and capture different perspectives, we applied data augmentation techniques. Rotation, horizontal flip, and vertical flip were employed to introduce diversity into the training set, ensuring that the models are exposed to a wide range of orientations and scenarios.

2) Model Selection and Training: In this phase, we conducted an exhaustive evaluation of eight pre-trained CNN models renowned for their efficacy in image classification tasks. The chosen models include ResNet101, DenseNet169, Xception, InceptionV3, DenseNet121, InceptionResNetV2, ResNet50, and EfficientNetB0. Our aim was to assess their performance in the context of retinal fundus image classification, considering their individual architectural nuances. Each selected model underwent a meticulous training process on our carefully prepared dataset. To ensure transparency and reproducibility, we documented the specific hyperparameters used for each model in a comprehensive Hyperparameter Tuning Table (Table 4). This table serves as a valuable reference, detailing the learning rates, batch sizes, optimizer choices, and other critical parameters tailored for optimal convergence of each respective model. Throughout the training process, we closely monitored convergence patterns, loss curves, and validation metrics to ascertain the models’ learning dynamics. This careful evaluation ensures that the models are not only capable of accurately classifying retinal fundus images but also possess the adaptability to generalize well to unseen data.

3) Explainable AI Techniques: We employed a suite of cutting-edge techniques, namely Grad-CAM, Grad-CAM++, Score-CAM, Faster Score-CAM, and LayerCAM. Each technique offers a unique perspective on model interpretability by highlighting the regions of the input image that significantly influence the model’s prediction. This integration is crucial for unveiling the hidden patterns and features that guide the models’ decisions, allowing for a more transparent understanding of their functionality. After successfully training our pre-trained CNN models on the retinal fundus dataset, we applied the Explainable AI techniques to delve into the decision-making mechanisms embedded within each model. These techniques generate heatmaps, visually indicating the regions of the input images that contribute most to the model’s predictions. By overlaying these heatmaps onto the original fundus images, we obtain a qualitative visualization of the features that hold significance in the classification process.

Figure 8 visually presents XAI images, showcasing heat maps overlaid onto original fundus images, illustrating the significant features influencing the classification process. This qualitative visualization enhances interpretability and aids in unraveling the intricacies of the models’ decision mechanisms.

4) Model Evaluation: In evaluating our pre-trained CNN models for fundus image classification, a diverse set of metrics was employed, each offering unique insights into predictive capabilities. After calculating metrics such as Accuracy, Precision, Recall, F1 Score, Jaccard Score, and Log Loss for each model, a meticulous analysis ensued. This examination provided valuable insights into models’ performance across various dimensions, enabling the identification of strengths and areas for improvement. The results of this comprehensive evaluation are presented in Table 7, shedding light on each model’s proficiency in overall accuracy, precision-recall balance, and resilience to dataset imbalances.

6.2 Pipeline 2: Retinal Blood Vessel Segmentation

1) Dataset Preparation: In this pivotal step, datasets meticulously tailored for retinal blood vessel segmentation were curated, encompassing the entirety of the FIVES and DRIVE datasets. The chosen datasets were then preprocessed to conform to the specific requirements of the task. All images from the FIVES and DRIVE datasets were resized uniformly to a dimension of 224x224 pixels, optimizing them for compatibility with segmentation models.

2) Exploration of Advanced UNet Models for Retinal Blood Vessel Segmentation: Our research delved into ten distinctive variations of medical image segmentation models¹, focusing on two prominent architectures: TransUNet and Attention U-Net, each employing diverse backbones to enhance performance. For the TransUNet approach, we explored the use of ResNet50V2, ResNet101V2, and

¹<https://github.com/yingkaisha/keras-unet-collection>

ResNet152V2 as backbones. Concurrently, within the Attention U-Net framework, we investigated the impact of using DensNet121, DensNet169, DensNet201, ResNet50V2, ResNet101V2, and ResNet152V2 as alternative backbones. Additionally, we examined the Swin-Unet model. Our primary objective was the segmentation of retinal blood vessels, a crucial task in medical image analysis. We meticulously conducted training and evaluation processes for each model, seeking optimal performance and insights into the comparative strengths of different backbones. Each selected model underwent thorough training on our carefully prepared dataset. To ensure transparency and reproducibility, we documented specific hyperparameters in a comprehensive Hyperparameter Tuning Table (Table 5 & Table 6). This table serves as a valuable reference, delineating learning rates, batch sizes, optimizer choices, and other critical parameters tailored for the optimal convergence of each respective model.

3) Model Evaluation: The segmentation models for Retinal Blood Vessel Segmentation were assessed using key metrics, including Intersection over Union (IoU), Dice Coefficient, Mean Pixel Accuracy, Mean Modified Hausdorff Distance, and Mean Surface Dice Overlap. Table 8 and Table 9 offers a thorough assessment of these indicators along with a detailed breakdown of the models' functionality.

7 Experiments

7.1 Experimental Setup

The experiment was carried out in three different environments, which include two instances used Jupyter Notebook environments, and the third used Kaggle. One Jupyter Notebook setup employed an NVIDIA GeForce RTX 3050 GPU (compute capability 8.6), an Intel Core i5 9400f CPU, and 16 GB of RAM. The other Jupyter Notebook environment boasted a more powerful NVIDIA GeForce RTX 3060 Ti GPU (compute capability 8.6), an Intel Core i5 13600K CPU, and 32 GB of memory. Both Jupyter Notebook environments used Python version 3.8.18 with TensorFlow version 2.6.0. Kaggle, on the other hand, provided access to NVIDIA Tesla P100 GPUs (compute capability 6.0), Intel Xeon CPUs, and 12.72 GB of RAM. The Kaggle setup utilized Python 3.10.13 with TensorFlow version 2.15.0.

7.2 Hyper-parameter Settings

Table 4 provides the hyperparameter settings for eight Pretrained CNNs models to classify fundus images. Every model was trained with a batch size ranging from 8 to 12, an Adam optimizer, and a learning rate ranging from 0.0005 to 0.001, but not at the same epoch. ResNet101 and ResNet50 were trained with epochs ranging from 50 to 70, DenseNet169 and DenseNet121 with epochs ranging from 40 to 60, InceptionV3 with epochs ranging from 60 to 80, ResNet50 with epochs ranging from 40 to 60, InceptionResNetV2 with epochs ranging from 30 to 40, and EfficientNetB0

Table 4: Hyperparameter Tuning for Fundus Image Classification Using Pretrained CNNs for FIVES dataset

Models	Learning Rate	Batch Size	Number of Epochs	Optimizer
ResNet101	0.001	10	60	Adam
DenseNet169	0.001	10	50	Adam
Xception	0.001	10	80	Adam
InceptionV3	0.001	10	70	Adam
DenseNet121	0.001	10	50	Adam
InceptionResNetV2	0.001	10	36	Adam
ResNet50	0.001	10	60	Adam
EfficientNetB0	0.001	10	120	Adam

Table 5: Hyperparameter Tuning for Retinal Blood Vessel Segmentation using U-Net Variants with Different Backbone Architectures for FIVES dataset

Models	Backbone	Learning Rate	Batch Size	Number of Epochs	Optimizer
TransUNET	ResNet50V2	0.001	4	80	Adam
	ResNet101V2	0.001	4	80	Adam
	ResNet152V2	0.001	4	80	Adam
Attention U-Net	ResNet50V2	0.001	4	65	Adam
	ResNet101V2	0.001	4	65	Adam
	ResNet152V2	0.001	4	65	Adam
	DenseNet121	0.001	4	65	Adam
	DenseNet169	0.001	4	65	Adam
	DenseNet201	0.001	4	65	Adam
Swin-UNET	Swin Transformer	0.001	4	100	Adam

with epochs ranging from 100 to 140. We employ ranges for epochs, learning rate, and batch size to showcase the diversity in training parameters, thereby ensuring the robustness of model performance. Nonetheless, in the table, we present exact values to uphold clarity and precision.

On the other hand, Table 5 and Table 6 represent hyperparameter settings for the Retinal Blood Vessel Segmentation for the FIVES and DRIVE dataset. We used three models, namely TransUnet, Attention U-Net, and Swin-UNET for both datasets. For FIVES and DRIVE, ResNet50V2, Resnet101V2, and Resnet152v2 were used as backbones for TransUNET and trained over a range of 80 to 100 epochs respectively. Furthermore, ResNet50V2, Resnet101V2, Resnet152V2, DenseNet121, DenseNet169, and DenseNet201 were used as backbones for Attention U-Net for both datasets with epochs ranging from 65 to 80. Lastly, Swin Transformer was used for Swin-UNET and trained with a range of 80 to 100 epochs for both datasets. All the models were experimented with a learning rate ranging from 0.001 to 0.01, a batch size ranging from 2 to 8, and an Adam optimizer. We use ranges for epochs, learning rate, and batch size to showcase the flexibility and variability in training parameters. However, in the table, we provide exact values to maintain clarity and precision.

Table 6: Hyperparameter Tuning for Retinal Blood Vessel Segmentation using U-Net Variants with Different Backbone Architectures for DRIVE dataset

Models	Backbone	Learning Rate	Batch Size	Number of Epochs	Optimizer
TransUNET	ResNet50V2	0.001	4	100	Adam
	ResNet101V2	0.001	4	100	Adam
	ResNet152V2	0.001	4	100	Adam
Attention U-Net	ResNet50V2	0.001	4	80	Adam
	ResNet101V2	0.001	4	80	Adam
	ResNet152V2	0.001	4	80	Adam
	DenseNet121	0.001	4	80	Adam
	DenseNet169	0.001	4	80	Adam
	DenseNet201	0.001	4	80	Adam
Swin-UNET	Swin Transformer	0.001	4	100	Adam

8 Interpretation of Results

8.1 Retinal Fundus Classification

Table 7 provides a comprehensive comparison of various fundus image classification models, showcasing their performance across different evaluation metrics. Each row corresponds to a specific model, with columns representing various evaluation metrics used for assessment. These metrics encompass accuracy, precision, recall, F1 score, Jaccard score, and log loss, collectively offering insights into the models' classification capabilities. Among the listed models, ResNet101 stands out as the top performer across multiple metrics. It achieves the highest accuracy of 94.17%, indicating superior overall classification performance compared to other models. With a precision score of 0.9435, ResNet101 exhibits strong capability in minimizing false positive predictions. Its recall score of 0.9417 reflects effectiveness in capturing positive instances within the dataset. Notably, ResNet101 also achieves a remarkable F1 score of 0.9418, striking a balance between precision and recall. Furthermore, its high Jaccard score of 0.8902 indicates strong similarity between predicted and true classifications. ResNet101 demonstrates a high level of confidence in its predictions, as evidenced by its low log loss value of 0.2254, signifying well-calibrated probability estimates. On the other hand, EfficientNetB0 emerges as the least performing model, with an accuracy of 88.33% and a relatively higher log loss of 0.6697, indicating less confidence in its predictions compared to higher-performing models like ResNet101. The models in the table are arranged from the highest (ResNet101) to the lowest (EfficientNetB0) values for clarity and comparison. Additionally, the confusion matrices corresponding to these models can be found in Figure 4, while Figure 5 depicts the loss and accuracy of training and validation data for all CNN models.

Table 7: Performance Evaluation of Pretrained CNNs for Fundus Image Classification

Model	Accuracy	Precision	Recall	F1 Score	Jaccard Score	Log Loss
ResNet101	0.9417	0.9435	0.9417	0.9418	0.8902	0.2254
DenseNet169	0.9333	0.9378	0.9333	0.9333	0.8751	0.9080
Xception	0.9250	0.9284	0.9250	0.9252	0.8612	1.3931
InceptionV3	0.9167	0.9203	0.9167	0.9166	0.8480	0.8012
DenseNet121	0.9083	0.9092	0.9083	0.9075	0.8320	4.5509
InceptionResNetV2	0.9000	0.9049	0.9000	0.9008	0.8202	12.0282
ResNet50	0.8917	0.8948	0.8917	0.8926	0.8089	0.4883
EfficientNetB0	0.8833	0.8862	0.8833	0.8837	0.7947	0.6697

8.2 Retinal Blood Vessel Segmentation

Table 8 and 9 presents the segmentation of blood vessels in fundus images employing various U-Net architectures, with Table 8 utilizing the DRIVE dataset and Table 9 utilizing the FIVES dataset. TransUNET, Attention U-Net, and Swin-UNET, the three fundamental U-Net architectures are compared. Various backbone architectures are utilized in these models. TransUNET utilize ResNet50V2, ResNet101V2, and ResNet152V2 as CNN backbones, while Attention U-Net integrates ResNet50V2, ResNet101V2, and ResNet152V2, as well as DenseNet121, DenseNet169, and DenseNet201 as backbones. Conversely, Swin-UNET utilizes the novel Swin Transformer as its backbone. Multiple evaluation metrics are employed to evaluate the performance of each model, including IoU (Intersection over Union), Dice Coefficient, Mean Pixel Accuracy, Mean Modified Hausdorff Distance, and Mean Surface Dice Overlap. On the DRIVE dataset, Attention U-Net with ResNet101V2 backbone achieves the highest IoU of 0.6483 and Dice score of 0.7865. Despite utilizing the novel Swin Transformer backbone, Swin-UNET demonstrates lower performance compared to other models, with an Intersection over Union (IoU) of 0.4896 and Dice score of 0.6569. Additionally, among the architectures, Attention U-Net with all its backbones outperforms the other two architectures, TransUNET and Swin-UNET. Similarly, on the FIVES dataset, we observe the same trends where Attention U-Net with all its backbones surpasses the other two architectures, TransUNET and Swin-UNET. Moreover, Attention U-Net with ResNet101V2 backbone attains the highest IoU of 0.7221 and Dice score of 0.8385. Conversely, Swin-UNET with the Swin Transformer as its backbone achieves the lowest IoU of 0.5179 and Dice score of 0.6765. So according to the results from both the DRIVE and FIVES datasets, Attention U-Net with ResNet101V2 as its backbone consistently outperforms other models in terms of segmenting blood vessels in fundus images. As a result, Attention U-Net with ResNet101V2 backbone is the most suitable model for this kind of task. Attention U-Net segmentation results for both the DRIVE and FIVES datasets using ResNet101V2 and ResNet152V2 are depicted in Figures 6 and 7, respectively.

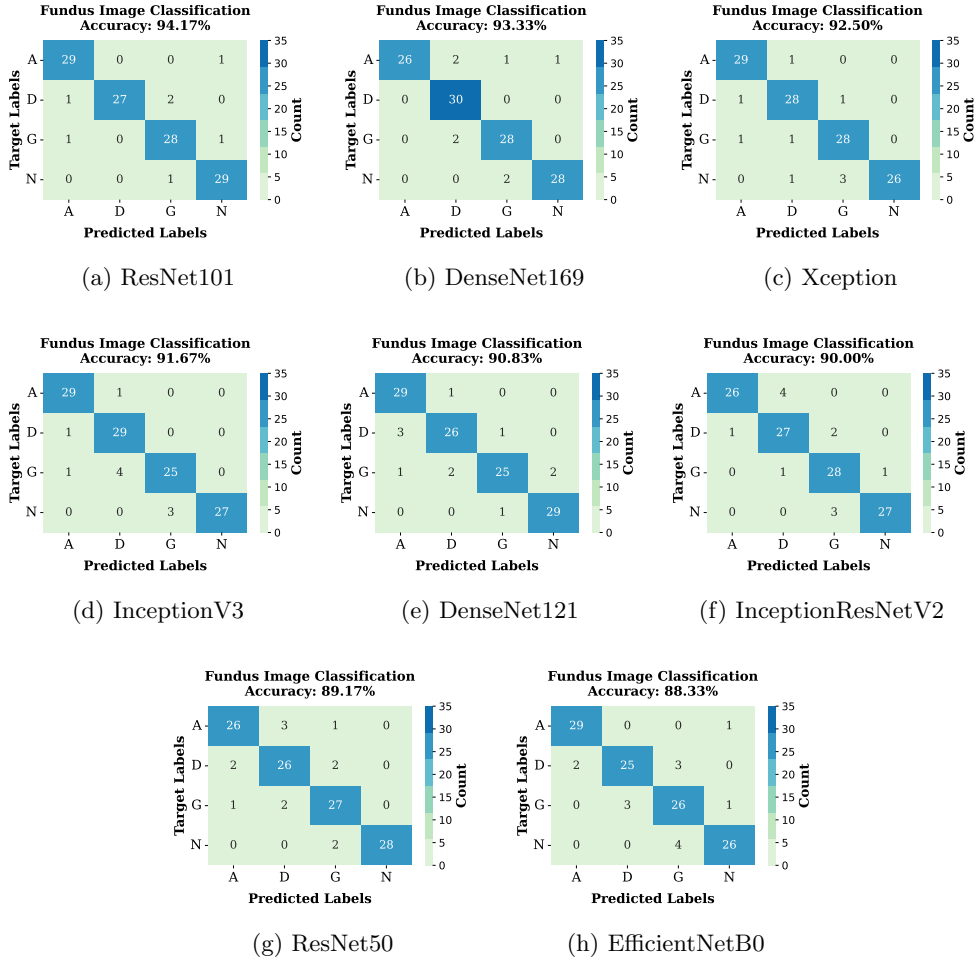


Fig. 4: Confusion Matrices of Pretrained CNNs for Retinal Fundus Classification

9 Discussion of Findings

9.1 Examining Methods of Explainable AI

Figure 8 shows the application of five explainable AI (XAI) methods Grad-CAM, Grad-CAM++, Score-CAM, Faster Score-CAM, and Layer CAM to classify fundus images using ResNet101 and DenseNet169 architectures. ResNet101 demonstrates strong performance across all XAI techniques, providing insightful visualizations of critical features contributing to classification decisions. Among the XAI methods, Score-CAM stands out for its effectiveness in highlighting relevant regions within the fundus images. However, DenseNet169 exhibits comparatively lower performance when

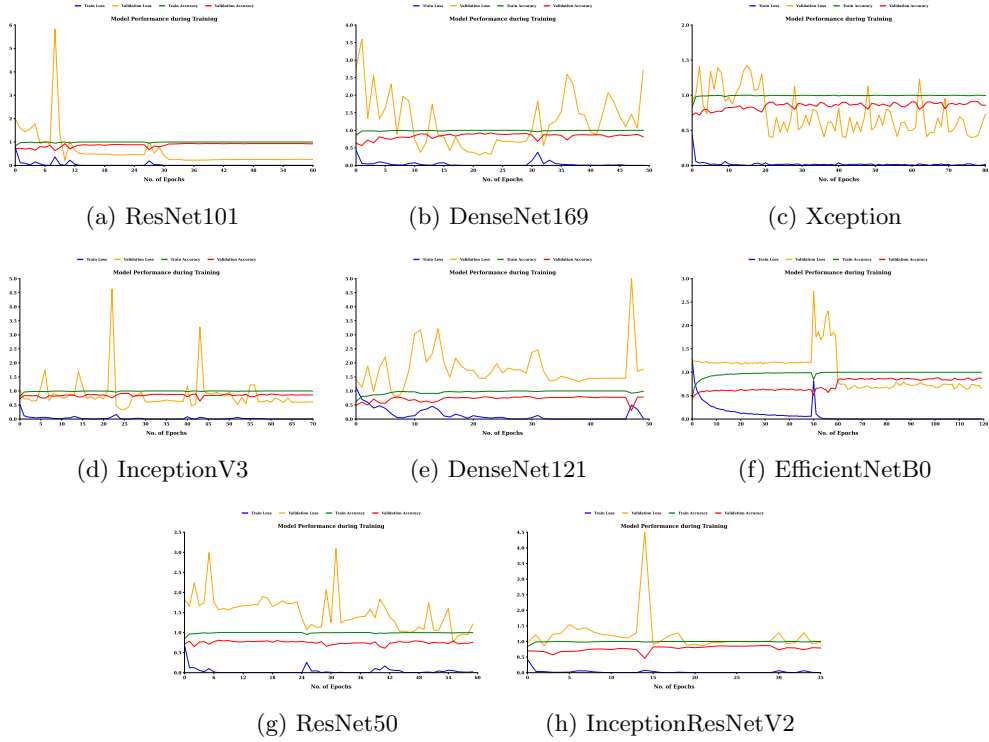


Fig. 5: Visualizing Pretrained CNN Models' Training and Validation Loss and Accuracy Graphs Across Epochs

compared to ResNet101, suggesting potential differences in the architectures interpretability and classification capabilities. This analysis highlights the significance of choosing suitable XAI methods customized to individual CNN architectures to achieve the best transparency and comprehension of deep learning models.

9.2 Comparative Performance Analysis

Table 10 provides a comparative analysis of our proposed models against existing studies conducted on DRIVE and FIVES datasets, focusing on Retinal Blood Vessel Segmentation Techniques. The Comparative Performance Analysis was conducted to evaluate the efficacy of our proposed Attention U-Net with ResNet101V2 model in the context of retinal blood vessel segmentation. By contrasting our results against existing studies conducted on DRIVE and FIVES datasets, we aimed to discern the strengths and weaknesses of our approach relative to established methodologies. This analysis provides valuable insights into the performance scape of retinal blood vessel segmentation techniques, highlighting the specific advantages our model offers. Through meticulous comparison with the findings of Wang et al. [53], Ko-Wei et al. [27], Ronneberge et al. [54], and Yan et al. [2], we can discern the relative performance

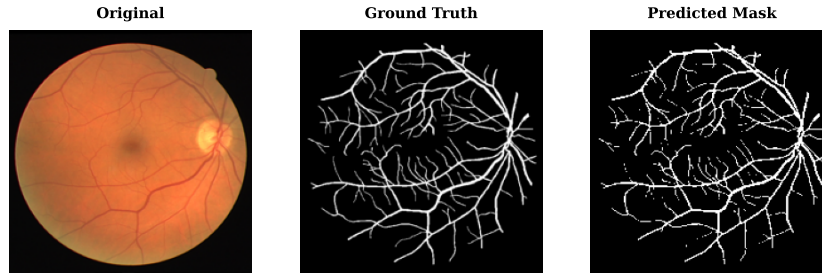
Table 8: U-Net Variants Performance Assessment for Retinal Blood Vessel Segmentation Using the DRIVE Dataset

Models	Backbone	Intersection over Union (IoU)	Dice Coefficient	Mean Pixel Accuracy	Mean Modified Hausdorff Distance	Mean Surface Dice Overlap
TransUNET	ResNet50V2	0.5273	0.6899	0.6470	3.852	0.0151
	ResNet101V2	0.5169	0.6803	0.6400	4.0864	0.0188
	ResNet152V2	0.5250	0.6879	0.6514	4.052	0.0167
Attention U-Net	ResNet50V2	0.6460	0.7848	0.7953	2.7150	0.0070
	ResNet101V2	0.6483	0.7865	0.8023	2.7341	0.0054
	ResNet152V2	0.6474	0.7859	0.7859	2.6718	0.0069
	DenseNet121	0.6427	0.7824	0.7747	2.7484	0.0090
	DenseNet169	0.6444	0.7837	0.7769	2.6776	0.0072
	DenseNet201	0.6422	0.7827	0.7749	2.6475	0.0074
Swin-UNET	Swin Transformer	0.4896	0.6569	0.6062	4.3675	0.0178

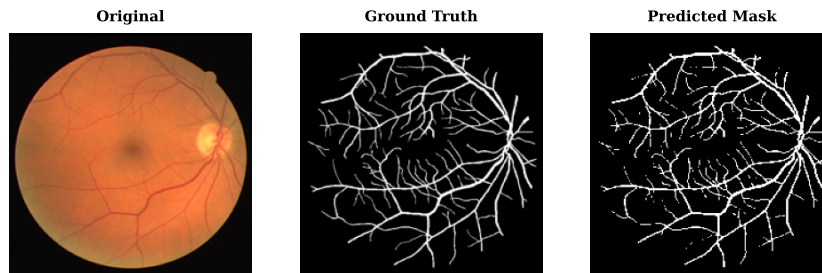
Table 9: U-Net Variants Performance Assessment for Retinal Blood Vessel Segmentation Using the FIVES Dataset

Models	Backbone	Intersection over Union (IoU)	Dice Coefficient	Mean Pixel Accuracy	Mean Modified Hausdorff Distance	Mean Surface Dice Overlap
TransUNET	ResNet50V2	0.6436	0.7791	0.7758	3.7392	0.0312
	ResNet101V2	0.6559	0.7898	0.7764	3.5491	0.0285
	ResNet152V2	0.6522	0.7866	0.7696	3.5278	0.0319
Attention U-Net	ResNet50V2	0.7175	0.8353	0.8512	2.8913	0.0201
	ResNet101V2	0.7221	0.8385	0.8507	2.8009	0.0223
	ResNet152V2	0.7199	0.8369	0.8331	2.8134	0.0378
	DenseNet121	0.6872	0.8143	0.7866	3.2814	0.0591
	DenseNet169	0.6718	0.8024	0.8115	3.5513	0.0235
	DenseNet201	0.6468	0.7822	0.7587	3.6267	0.0293
Swin-UNET	Swin Transformer	0.5179	0.6765	0.5987	4.6090	0.0891

metrics such as Dice Coefficient and Intersection over Union achieved by each method. Our proposed Attention U-Net with ResNet101V2 achieved an Intersection over Union of 64.83 and a Dice Coefficient of 78.65 on the DRIVE dataset. Such comparisons are essential for understanding the state-of-the-art in this domain and for gauging the potential impact of our proposed model. By demonstrating superior performance, particularly evident in the higher Dice Coefficient values obtained on both the DRIVE and FIVES datasets, we establish the competitive edge of our Attention U-Net with ResNet101V2 model. Therefore, through this Comparative Performance Analysis, we



(a) Attention U-Net: ResNet101V2



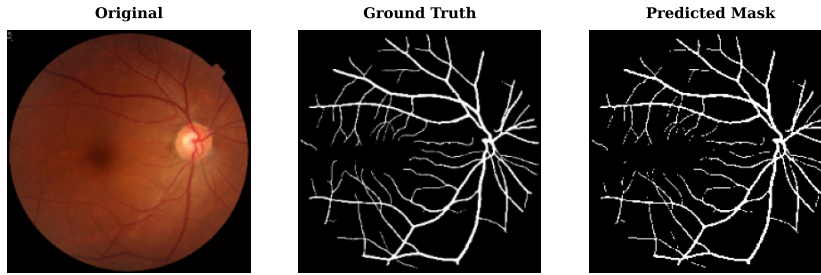
(b) Attention U-Net: Resnet152V2

Fig. 6: Comparison of Attention U-Net models for retinal blood vessel segmentation on the DRIVE dataset using (a) ResNet101V2 as Backbone and (b) ResNet152V2 architectures as Backbone.

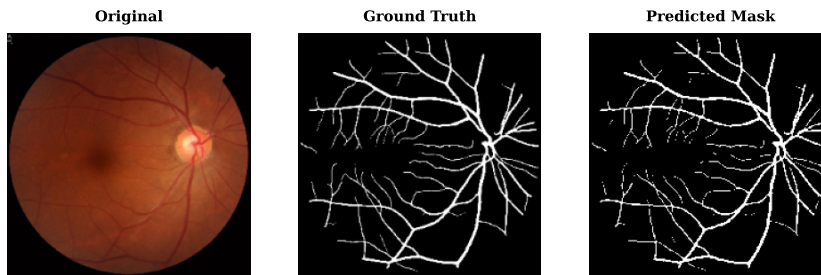
aim to validate and underscore the significance of our contributions to retinal blood vessel segmentation, ultimately advocating for the adoption of our proposed model as a robust and effective solution in this field.

10 Limited Areas of Investigation

One significant drawback in the field of retinal fundus classification is the inability of pre-trained CNN models to be applied to datasets with small quantities of data, which results in inconsistent performance. Enhancing model transferability with fewer datasets is a difficulty that has to be addressed through research, and doing so will greatly advance the discipline. Despite the use of XAI approaches, another area of concern is the interpretability of model choices. Subsequent studies may focus on improving the XAI outputs' comprehensibility and interpretability in order to promote a better comprehension of the decision-making procedures. Turning our attention



(a) Attention U-Net: ResNet101V2



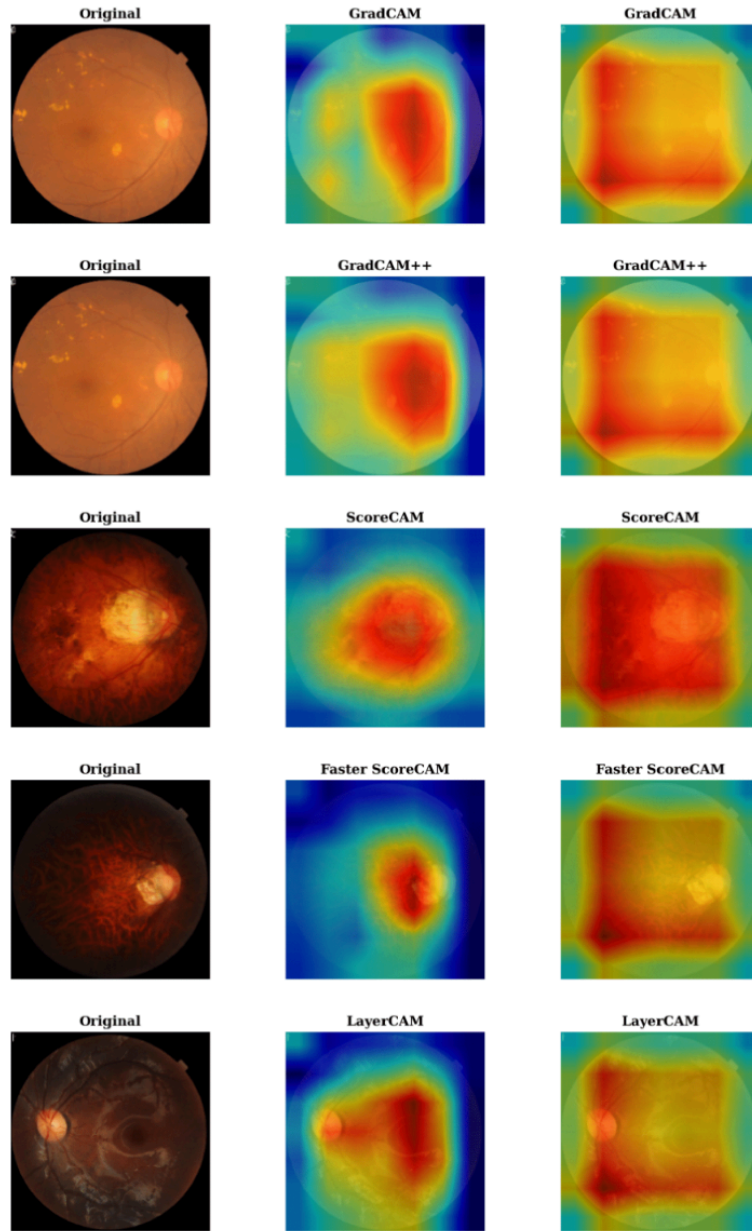
(b) Attention U-Net: Resnet152V2

Fig. 7: Comparison of Attention U-Net models for retinal blood vessel segmentation on the FIVES dataset using (a) ResNet101V2 architectures as Backbone and (b) ResNet152V2 architectures as Backbone.

to retinal blood vessel segmentation, difficulties occur when handling complex vascular systems, particularly when there are overlapping veins or abnormalities present. Addressing these intricacies is essential to improving segmentation precision. Furthermore, the reliance of segmentation models on picture quality poses a limitation, necessitating further investigation to develop approaches for managing differences stemming from various imaging equipment or acquisition configurations. Moreover, the restricted application of segmentation models to a wide range of retinal disorders emphasizes the need to grow datasets to encompass a variety of diseased states and anatomical variances, hence improving the model's overall usefulness.

11 Potential Areas for Further Investigation

Future studies in the field of retinal fundus classification may concentrate on investigating ensemble learning strategies to increase generalization and robustness. By utilizing



a) Original Image b) ResNet101 c) DenseNet169

Fig. 8: Comparative Analysis of Explainable AI Methods on Fundus Image Classification: Highlighting the 1st Highest Performance Achieved with ResNet101 (b) and the 2nd Highest with DenseNet169 (c), and the Effectiveness of Gradient-Based Explainable AI Techniques for Insightful Visualization. Additionally, (a) Original Image is provided for reference.

Table 10: Comparison of performance with other studies conducted on the DRIVE and FIVES dataset

Dataset	Paper	Model	Metric	Score	Our Proposed Approach
DRIVE	Wang et al. [53]	UNet++	Dice Coefficient	78.63	78.65 (Attention U-Net)
	Ko-Wei et al. [27]	Custom U-Net	Intersection over Union	60.80	64.83 (Attention U-Net)
FIVES	Ronneberger et al. [54]	U-Net	Dice Coefficient	81.74	83.85 (Attention U-Net)
	Yan et al. [2]	Custom U-Net	Dice Coefficient	81.65	

the advantages of various CNN architectures, ensemble techniques might lead to better performance. Furthermore, fine-tuning pre-trained models domain-specifically on fundus image datasets customized to the distinct features of retinal images may result in more accurate and clinically meaningful classification results. Another approach worth looking into is integrating clinical metadata, such as patient demographics and medical history, into the classification pipeline. This might lead to a more comprehensive knowledge and possibly improve diagnosis accuracy. By broadening the focus, a number of recently developed methods may greatly enhance retinal fundus classification: Firstly, the investigation of generative models for the synthesis of retinal fundus images may enrich datasets, particularly in situations when data is few, improving the generalization of models. Second, a fresh approach that could shed light on the benefits and advantages of Vision Transformers (ViTs) and its variations over traditional CNN designs is to look at how they might be used for retinal fundus classification. Finally, investigation into diffusion models for retinal fundus classification is a fascinating field with the potential to increase classification accuracy by identifying intricate data dependencies. In the domain of retinal blood vessel segmentation, additional future research directions include exploring multi-modal fusion techniques to gain a more comprehensive understanding of retinal vascular structures, investigating semi-supervised learning methods to address data scarcity, and adapting segmentation models for real-time applications in clinical settings to improve patient care and diagnosis.

12 Conclusion

In conclusion, by carefully analyzing retinal blood vessels in fundus images, our research offers an important breakthrough in the field of early disease identification. We have undertaken a complex and varied journey, studying two different pipelines that have made a significant contribution to our understanding and interpretation of these images. We have combined eight popular pre-trained CNN models with the power of eXplainable AI (XAI) in our first pipeline. In addition to allowing fast image classification, this strategic fusion opens the door to these models' invisible workings and provides straightforward reasons for the classifications that were made. This method greatly increases confidence in the underlying decision-making processes of these models, improving their overall usability and dependability. In the second pipeline, we use Attention U-Net, Trans U-Net, and Swin-UNET designs to the complex area of retinal blood vessel segmentation. By use of careful segmentation, we reveal the complex

network of blood vessels present in fundus images, enhancing our understanding of the vascular system. Our evaluation of fundus image classification highlights compelling insights into the performance of various CNN models. Notably, ResNet101 emerges as the top-performing model, achieving an impressive accuracy of 94.17%, while EfficientNetB0 demonstrates comparatively lower performance, with a score of 88.33%. Moreover, our exploration encompasses diverse architectures and techniques, including Attention U-Net models with reputable backbones, TransUNet, and Swin-Unet, each offering unique perspectives on fundus image analysis. By quantifying the performance of these models through various metrics, we provide valuable benchmarks for future research endeavors. Notably, our findings showcase the efficacy of Swin-Unet, achieving a maximum Dice Coefficient of 0.8993, while TransUNet with ResNet50V2 backbone exhibits a minimum Dice Coefficient of 0.7791.

Authors' contributions

Faria and Mukaffi delineated the research objectives, conducted comprehensive studies, executed coding processes, supervised the primary experiments, and took the lead in drafting the manuscript. Pronay assisted in manuscript writing, conducted multiple experiments, evaluated writing quality, and rectified grammatical errors. Fahim contributed to manuscript writing, conducted multiple experiments, and performed analysis. Faisal provided essential supervision and guidance throughout the research, shaping its direction, and critically edited the manuscript.

Declarations

Ethical Approval and Consent to participate

Not Applicable.

Human and Animal Ethics

Not Applicable.

Code Availability

The code and supporting files for this study, publicly accessible for reference and use, can be found on GitHub at: <https://github.com/fatemafaria142/Retinal-Fundus-Classification-using-XAI-and-Segmentation>

Conflicts of Interest

The authors declare that they have no conflicts of interest.

Funding

This research was carried out with no external funding.

References

- [1] Y. Jang, J. Son, K. Park, S.J. Park, K.H. Jung, Laterality classification of fundus images using interpretable deep neural network. *Journal of Digital Imaging* **31** (2018). <https://doi.org/10.1007/s10278-018-0099-2>
- [2] Y. Pan, J. Liu, Y. Cai, X. Yang, Z. Zhang, H. Long, K. Zhao, X. Yu, C. Zeng, J. Duan, P. Xiao, J. Li, F. Cai, X. Yang, Z. Tan, Fundus image classification using inception v3 and resnet-50 for the early diagnostics of fundus diseases. *Frontiers in Physiology* **14**, 1126780 (2023). <https://doi.org/10.3389/fphys.2023.1126780>
- [3] M. Mateen, J. Wen, D. Nasrullah, S. Song, Z. Huang, Fundus image classification using vgg-19 architecture with pca and svd. *Symmetry* **11**, 1 (2018). <https://doi.org/10.3390/sym11010001>
- [4] Y. Katada, N. Ozawa, K. Masayoshi, Y. Ofuji, K. Tsubota, T. Kurihara, Automatic screening for diabetic retinopathy in interracial fundus images using artificial intelligence. *Intelligence-Based Medicine* **3-4**, 100024 (2020). <https://doi.org/10.1016/j.ibmed.2020.100024>
- [5] W. Alyoubi, M. Abulkhair, W. Shalash, Diabetic retinopathy fundus image classification and lesions localization system using deep learning. *Sensors* **21**, 3704 (2021). <https://doi.org/10.3390/s21113704>
- [6] T. Saba, S. Bokhari, M. Sharif, Y. Mussarat, M. Raza, Fundus image classification methods for the detection of glaucoma: A review. *Microscopy research and technique* **81** (2018). <https://doi.org/10.1002/jemt.23094>
- [7] C. Liu, X. Han, Z. Li, J. Ha, G. Peng, W. Meng, M. He, A self-adaptive deep learning method for automated eye laterality detection based on color fundus photography. *PLOS ONE* **14**, e0222025 (2019). <https://doi.org/10.1371/journal.pone.0222025>
- [8] K. Kyoung Min, T.Y. Heo, A. Kim, J. Kim, K. Han, J. Yun, J.K. Min, Development of a fundus image-based deep learning diagnostic tool for various retinal diseases. *Journal of Personalized Medicine* **11**, 321 (2021). <https://doi.org/10.3390/jpm11050321>
- [9] Y. Kim, K. Noh, S. Byun, S. Lee, T. Kim, L. Sunwoo, K. Lee, S.H. Kang, K. Park, S.J. Park, Effects of hypertension, diabetes, and smoking on age and sex prediction from retinal fundus images. *Scientific Reports* **10** (2020). <https://doi.org/10.1038/s41598-020-61519-9>
- [10] Y. Jiang, F. Wang, J. Gao, S. Cao, Multi-path recurrent u-net segmentation of retinal fundus image. *Applied Sciences* **10**(11) (2020). <https://doi.org/10.3390/app10113777>. URL <https://www.mdpi.com/2076-3417/10/11/3777>

- [11] N. Memari, A.R. Ramli, M.I. Saripan, S. Mashohor, M. Moghbel, Retinal blood vessel segmentation by using matched filtering and fuzzy c-means clustering with integrated level set method for diabetic retinopathy assessment. *Journal of Medical and Biological Engineering* **39**, 713–731 (2019). <https://doi.org/10.1007/s40846-018-0454-2>
- [12] A. Kind, G. Azzopardi, *An Explainable AI-Based Computer Aided Detection System for Diabetic Retinopathy Using Retinal Fundus Images* (2019), pp. 457–468. https://doi.org/10.1007/978-3-030-29888-3_37
- [13] Z. Chen, W. Jin, X. Zeng, L. Xu, Retinal vessel segmentation based on task-driven generative adversarial network. *IET Image Processing* **14** (2021). <https://doi.org/10.1049/iet-ipr.2020.1032>
- [14] A.A. Abdulsahib, M.A. Mahmoud, H. Aris, S.S. Gunasekaran, M.A. Mohammed, An automated image segmentation and useful feature extraction algorithm for retinal blood vessels in fundus images. *Electronics* **11**(9) (2022). <https://doi.org/10.3390/electronics11091295>. URL <https://www.mdpi.com/2079-9292/11/9/1295>
- [15] M. Mateen, J. Wen, Nasrullah, S. Song, Z. Huang, Fundus image classification using vgg-19 architecture with pca and svd. *Symmetry* **11**(1) (2019). <https://doi.org/10.3390/sym11010001>. URL <https://www.mdpi.com/2073-8994/11/1/1>
- [16] A.O. Asia, C.Z. Zhu, S.A. Althubiti, D. Al-Alimi, Y.L. Xiao, P.B. Ouyang, M.A.A. Al-Qaness, Detection of diabetic retinopathy in retinal fundus images using cnn classification models. *Electronics* **11**(17) (2022). <https://doi.org/10.3390/electronics11172740>. URL <https://www.mdpi.com/2079-9292/11/17/2740>
- [17] Y. Pan, K. Zhao, Z. Tan, Fundus image classification using inception v3 and resnet-50 for the early diagnostics of fundus diseases. *Frontiers in Physiology* **14**, 1126780 (2023)
- [18] R. Thanki, A deep neural network and machine learning approach for retinal fundus image classification. *Healthcare Analytics* **3**, 100140 (2023). <https://doi.org/https://doi.org/10.1016/j.health.2023.100140>. URL <https://www.sciencedirect.com/science/article/pii/S2772442523000072>
- [19] Y. Katada, N. Ozawa, K. Masayoshi, Y. Ofuji, K. Tsubota, T. Kurihara, Automatic screening for diabetic retinopathy in interracial fundus images using artificial intelligence. *Intelligence-Based Medicine* **3-4**, 100024 (2020). <https://doi.org/https://doi.org/10.1016/j.ibmed.2020.100024>. URL <https://www.sciencedirect.com/science/article/pii/S2666521220300247>
- [20] G. Sun, X. Wang, L. Xu, C. Li, W. Wang, Z. Yi, H. Luo, Y. Su, J. Zheng, Z. Li, et al., Deep learning for the detection of multiple fundus diseases using ultra-widefield images. *Ophthalmology and Therapy* **12**(2), 895–907 (2023)

- [21] W. Li, Y. Xiao, H. Hu, C. Zhu, H. Wang, Z. Liu, A.K. Sangaiah, Retinal vessel segmentation based on b-cosfire filters in fundus images. *Frontiers in Public Health* **10**, 914973 (2022)
- [22] Y. Jiang, F. Wang, J. Gao, S. Cao, Multi-path recurrent u-net segmentation of retinal fundus image. *Applied Sciences* **10**(11) (2020). <https://doi.org/10.3390/app10113777>. URL <https://www.mdpi.com/2076-3417/10/11/3777>
- [23] P. Yin, R. Yuan, Y. Cheng, Q. Wu, Deep guidance network for biomedical image segmentation. *IEEE Access* **8**, 116106–116116 (2020). <https://doi.org/10.1109/ACCESS.2020.3002835>
- [24] S. David, C. Mahesh, D. Venkatesan, K. Polat, A. Alhudhaif, M. Nour, Retinal blood vessels and optic disc segmentation using u-net. *Mathematical Problems in Engineering* **2022**, 1–11 (2022). <https://doi.org/10.1155/2022/8030954>
- [25] C. Guo, M. Szemenyei, Y. Yi, W. Wang, B. Chen, C. Fan. Sa-unet: Spatial attention u-net for retinal vessel segmentation (2020)
- [26] M.S. Gargari, M.H. Seyedi, M. Alilou, Segmentation of retinal blood vessels using u-net++ architecture and disease prediction. *Electronics* **11**(21) (2022). <https://doi.org/10.3390/electronics11213516>. URL <https://www.mdpi.com/2079-9292/11/21/3516>
- [27] K.W. Huang, Y.R. Yang, Z.H. Huang, Y.Y. Liu, S.H. Lee, Retinal vascular image segmentation using improved unet based on residual module. *Bioengineering* **10**(6) (2023). <https://doi.org/10.3390/bioengineering10060722>. URL <https://www.mdpi.com/2306-5354/10/6/722>
- [28] K. Jin, X. Huang, J. Zhou, Y. Li, Y. Yan, Y. Sun, Q. Zhang, Y. Wang, J. Ye, Fives: A fundus image dataset for artificial intelligence based vessel segmentation. *Scientific Data* **9** (2022). <https://doi.org/10.1038/s41597-022-01564-3>
- [29] J. Staal, M. Abramoff, M. Niemeijer, M. Viergever, B. van Ginneken, Ridge-based vessel segmentation in color images of the retina. *IEEE Transactions on Medical Imaging* **23**(4), 501–509 (2004). <https://doi.org/10.1109/TMI.2004.825627>
- [30] R.R. Selvaraju, M. Cogswell, A. Das, R. Vedantam, D. Parikh, D. Batra, Grad-cam: Visual explanations from deep networks via gradient-based localization. *International Journal of Computer Vision* **128**(2), 336–359 (2019). <https://doi.org/10.1007/s11263-019-01228-7>. URL <http://dx.doi.org/10.1007/s11263-019-01228-7>
- [31] A. Chattopadhyay, A. Sarkar, P. Howlader, V.N. Balasubramanian, in *2018 IEEE Winter Conference on Applications of Computer Vision (WACV)* (IEEE, 2018). <https://doi.org/10.1109/wacv.2018.00097>. URL <http://dx.doi.org/10.1109/WACV.2018.00097>

- [32] H. Wang, Z. Wang, M. Du, F. Yang, Z. Zhang, S. Ding, P. Mardziel, X. Hu. Score-cam: Score-weighted visual explanations for convolutional neural networks (2019). <https://doi.org/10.48550/ARXIV.1910.01279>. URL <https://arxiv.org/abs/1910.01279>
- [33] J. Li, D. Zhang, B. Meng, Y. Li, L. Luo, Fimf score-cam: Fast score-cam based on local multi-feature integration for visual interpretation of cnns. *IET Image Processing* **17**(3), 761–772 (2022). <https://doi.org/10.1049/ipr2.12670>. URL <http://dx.doi.org/10.1049/ipr2.12670>
- [34] P.T. Jiang, C.B. Zhang, Q. Hou, M.M. Cheng, Y. Wei, Layercam: Exploring hierarchical class activation maps for localization. *IEEE Transactions on Image Processing* **30**, 5875–5888 (2021). <https://doi.org/10.1109/TIP.2021.3089943>
- [35] F. Li, L. Yan, Y. Wang, J. Shi, H. Chen, z. xuedian, M. Jiang, Z. Wu, K. Zhou, Deep learning-based automated detection of glaucomatous optic neuropathy on color fundus photographs. *Graefe’s Archive for Clinical and Experimental Ophthalmology* **258** (2020). <https://doi.org/10.1007/s00417-020-04609-8>
- [36] C.U. Kumari, A. Hemanth, V. Anand, D.S. Kumar, R. Naga Sanjeev, T.S. Sri Harshitha, in *2022 Third International Conference on Intelligent Computing Instrumentation and Control Technologies (ICICICT)* (2022), pp. 1312–1316. <https://doi.org/10.1109/ICICICT54557.2022.9917709>
- [37] F. Chollet. Xception: Deep learning with depthwise separable convolutions (2017)
- [38] C. Szegedy, V. Vanhoucke, S. Ioffe, J. Shlens, Z. Wojna, Rethinking the inception architecture for computer vision. *CoRR* **abs/1512.00567** (2015). URL <http://arxiv.org/abs/1512.00567>. [arXiv:1512.00567](https://arxiv.org/abs/1512.00567)
- [39] X. Li, X. Shen, Y. Zhou, X. Wang, T.Q. Li, Classification of breast cancer histopathological images using interleaved densenet with senet (idsnet). *PLOS ONE* **15**, e0232127 (2020). <https://doi.org/10.1371/journal.pone.0232127>
- [40] C. Szegedy, S. Ioffe, V. Vanhoucke, A. Alemi. Inception-v4, inception-resnet and the impact of residual connections on learning (2016)
- [41] K. He, X. Zhang, S. Ren, J. Sun. Deep residual learning for image recognition (2015)
- [42] C.H. Patel, D. Undaviya, H. Dave, S. Degadwala, D. Vyas, in *2023 2nd International Conference on Applied Artificial Intelligence and Computing (ICAAIC)* (2023), pp. 713–718. <https://doi.org/10.1109/ICAAIC56838.2023.10141195>
- [43] J. Chen, Y. Lu, Q. Yu, X. Luo, E. Adeli, Y. Wang, L. Lu, A.L. Yuille, Y. Zhou. Transunet: Transformers make strong encoders for medical image segmentation (2021)

- [44] O. Oktay, J. Schlemper, L.L. Folgoc, M. Lee, M. Heinrich, K. Misawa, K. Mori, S. McDonagh, N.Y. Hammerla, B. Kainz, B. Glocker, D. Rueckert. Attention u-net: Learning where to look for the pancreas (2018)
- [45] H. Cao, Y. Wang, J. Chen, D. Jiang, X. Zhang, Q. Tian, M. Wang. Swin-unet: Unet-like pure transformer for medical image segmentation (2021)
- [46] M. Sokolova, N. Japkowicz, S. Szpakowicz, (2006), pp. 1015–1021. https://doi.org/10.1007/11941439_114
- [47] J. Hancock, *Jaccard Distance (Jaccard Index, Jaccard Similarity Coefficient)* (2004). <https://doi.org/10.1002/9780471650126.dob0956>
- [48] H. Rezatofghi, N. Tsoi, J. Gwak, A. Sadeghian, I. Reid, S. Savarese, in *Proceedings of the IEEE/CVF Conference on Computer Vision and Pattern Recognition (CVPR)* (2019)
- [49] R.R. Shamir, Y. Duchin, J. Kim, G. Sapiro, N. Harel. Continuous dice coefficient: a method for evaluating probabilistic segmentations (2019)
- [50] X. Jiang, H. Yu, S. Lv, An image segmentation algorithm based on a local region conditional random field model. *International Journal of Communications, Network and System Sciences* **13**, 139–159 (2020). <https://doi.org/10.4236/ijcns.2020.139009>
- [51] O.U. Aydin, A.A. Taha, A. Hilbert, A.A. Khalil, I. Galinovic, J.B. Fiebach, D. Frey, V.I. Madai, On the usage of average hausdorff distance for segmentation performance assessment: hidden error when used for ranking. *European Radiology Experimental* **5**(1) (2021). <https://doi.org/10.1186/s41747-020-00200-2>. URL <http://dx.doi.org/10.1186/s41747-020-00200-2>
- [52] S. Nikolov, S. Blackwell, R. Mendes, J. Fauw, C. Meyer, C. Hughes, H. Askham, B. Romera-Paredes, A. Karthikesalingam, C. Chu, D. Carnell, C. Boon, D. D’souza, S. Moinuddin, K. Sullivan, D. Consortium, H. Montgomery, G. Rees, R. Sharma, O. Ronneberger, Deep learning to achieve clinically applicable segmentation of head and neck anatomy for radiotherapy (2018)
- [53] C. Wang, Z. Zhao, Y. Yu, Fine retinal vessel segmentation by combining nest u-net and patch-learning. *Soft Computing* **25**(7), 5519–5532 (2021). <https://doi.org/10.1007/s00500-020-05552-w>. URL <http://dx.doi.org/10.1007/s00500-020-05552-w>
- [54] O. Ronneberger, P. Fischer, T. Brox, in *Medical Image Computing and Computer-Assisted Intervention – MICCAI 2015*, ed. by N. Navab, J. Hornegger, W.M. Wells, A.F. Frangi (Springer International Publishing, Cham, 2015), pp. 234–241